Brief Communication

MOLECULAR METABOLISM

Hepatic FTO is dispensable for the regulation of metabolism but counteracts HCC development *in vivo*

Melanie J. Mittenbühler [1,2], Katarzyna Saedler [1,2], Hendrik Nolte [3], Lara Kern [1,2], Jun Zhou [4], Shu-Bing Qian [4], Lydia Meder [5,6], Roland T. Ullrich [5,6,7,8], Jens C. Brüning [1,2,6,], F. Thomas Wunderlich [1,2,6,*]**

ABSTRACT

Objective: Single-nucleotide polymorphisms in the FTO gene encoding an m^6Am and an m^6A demethylase are associated with obesity. Moreover, recent studies have linked a dysregulation of m^6A modifications and its machinery, including FTO, to the development of several forms of cancers. However, the functional role of hepatic FTO in metabolism and the development and progression of hepatocellular carcinoma (HCC), a proteotypic obesity-associated cancer, remains unclear. Thus, we aimed to reveal the role of hepatic FTO in metabolism and in the initiation and progression of HCC *in vivo*.

Methods: We generated mice with hepatic FTO deficiency (FTO^{L-KO}). The effect of hepatic FTO on metabolism was investigated by extensive metabolic phenotyping. To determine the impact of hepatic FTO on HCC development, FTO^{L-KO} and Ctrl mice were subjected to long-term diethylnitrosamine (DEN)-induced HCC-development and the tumor initiation phase was examined via a short-term DEN protocol.

Results: In long-term DEN experiments, FTO^{L-KO} mice exhibit increased HCC burden compared to Ctrl mice. In the tumor initiation phase, Ctrl mice display a dynamic regulation of FTO upon induction of liver damage, while this response is abrogated in FTO-deficient mice. Proteomic analyses revealed that liver damage-induced increases in FTO expression reduce CUL4A protein abundance. Functionally, simultaneous knockdown of *Cul4a* reverses the increased hepatocyte proliferation observed upon loss of FTO.

Conclusion: Collectively, our study demonstrates that hepatic FTO is dispensable for the control of energy homeostasis and glucose metabolism. However, we show a protective function of FTO in liver carcinogenesis and suggest the FTO-dependent dynamic mRNA demethylation of *Cul4a* in the initiation of HCC development contributes to this effect.

Keywords Hepatocellular carcinoma; FTO; Cul4a; m^6A

1. INTRODUCTION

Obesity represents an increasing health burden in western societies. The worldwide prevalence more than doubled since 1980 and is continuously increasing [1]. Overweight and obesity are not only major drivers for the development of numerous diseases, such as type 2 diabetes mellitus and cardiovascular diseases but also predispose patients to different forms of cancer [2–5]. Notably, the relative risk of dying from cancer is increased upon obesity, and among all cancer types, liver cancer displays the highest mortality risk of males with increased body mass index (BMI) in the U.S. [4,6]. Hepatocellular carcinoma (HCC) is a malignant transformation of hepatocytes and one of the most frequent causes of cancer death worldwide [7,8]. In light of the growing numbers of obese individuals, HCC incidences are expected to further increase, and thereby novel therapeutic approaches are urgently needed to combat this fatal disease.

Single-nucleotide polymorphisms (SNP) in the fat mass and obesity-associated (*FTO*) gene have been shown to predispose to obesity in humans [9–14]. FTO-deficient mice display decreased bodyweight and adipose tissue, due to an increase in energy expenditure [13], whereas overexpression of FTO increases food intake and causes obesity in mice [14]. In light of these findings, FTO seems to be a promising target for therapeutic approaches to treat obesity and its

[1]Max Planck Institute for Metabolism Research, Center for Endocrinology, Diabetes and Preventive Medicine (CEDP), Cologne, 50931, Germany [2]Excellence Cluster on Cellular Stress Responses in Aging Associated Diseases (CECAD), Germany [3]Max Planck Institute for Biology of Ageing, Cologne, 50931, Germany [4]Division of Nutritional Sciences, Cornell University, Ithaca, NY, 14853, USA [5]Department I of Internal Medicine, University Hospital Cologne, Cologne, 50931, Germany [6]Center for Molecular Medicine Cologne, University of Cologne, Cologne, 50931, Germany [7]Center for Integrated Oncology Cologne/Bonn, University Hospital Cologne, 50931, Cologne, Germany [8]University Hospital Bonn, Bonn, 53172, Germany

*Corresponding author. Max Planck Institute for Metabolism Research, Center for Endocrinology, Diabetes and Preventive Medicine (CEDP), Cologne, 50931, Germany; Excellence Cluster on Cellular Stress Responses in Aging Associated Diseases (CECAD), Germany. E-mail: bruening@sf.mpg.de (F.T. Wunderlich).

**Corresponding author. Max Planck Institute for Metabolism Research, Center for Endocrinology, Diabetes and Preventive Medicine (CEDP), Cologne, 50931, Germany; Excellence Cluster on Cellular Stress Responses in Aging Associated Diseases (CECAD), Germany. E-mail: thomas.wunderlich@sf.mpg.de (J.C. Brüning).

Received April 18, 2020 • Revision received September 15, 2020 • Accepted September 16, 2020 • Available online 19 September 2020

https://doi.org/10.1016/j.molmet.2020.101085

associated diseases. However, more recently, SNPs within the FTO gene have been found to impinge on other, more distal genes rather than affecting FTO expression itself [15–18]. In detail, regions within the *FTO* gene have been found to interact with regulatory elements of the *IRX3* gene, and *Irx3* inactivation protects mice against diet-induced weight gain [15]. Furthermore, the *RPGRIP1L* gene, located close to the transcriptional start site of *FTO*, is also affected by these SNPs and hypomorphic *Rpgrip1l* mice are hyperphagic and obese [16–18]. Therefore, obesity-associated SNPs may affect expression of other genes to dysregulate metabolism in obesity. However, given the severe metabolic alterations observed in mouse models of FTO deficiency and overexpression, which do not influence the intronic regions of obesity-associated SNPs, FTO itself is likely to also play a role in the regulation of metabolism.

FTO belongs to the superfamily of alpha-ketoglutarate-dependent hydroxylases and was the first identified demethylase that catalyzes not only demethylation of thymidine and uracil bases in DNA, but also of N6,2′O-dimethyladenosine (m^6Am) and N6-Methyladenosine (m^6A) modifications in snRNAs and mRNAs [19–22]. m^6Am at +1 A adjacent to the m^7G cap of snRNAs is the preferred target of FTO [23]. Nevertheless, m^6Am and m^6A are both demethylated by FTO, although m^6A to a 100-fold lower extent than m^6Am [24].

The highly abundant m^6A mRNA modifications are dynamically regulated through a machinery of m^6A writers, readers, and erasers [22,25–27]. The m^6A methyltransferase complex – referred to as m^6A writer – is composed of methyltransferase-like 3 and 14 (METTL3 and METTL14), and their cofactors Wilms tumor-1-associated protein (WTAP), VIRMA (KIAA1429), and RBM15. m^6A modifications are directly recognized by so-called readers, which are members of the YT521-B homology (YTH)-domain family. Depending on the reader, an m^6A modification can either result in the promotion of mRNA translation or induction of mRNA decay [28–30]. Additionally, m^6A readers can impact splicing, nuclear export, and stability of mRNAs [31,32]. m^6A modifications can be removed by so called erasers or m^6A demethylases, such as FTO and ALKBH5 [21,33,34]. The best characterized demethylase is FTO, which is highly expressed in the brain, where it critically regulates dopaminergic neurocircuits and locomotor activity [35–37]. However, FTO expression is not only restricted to the brain, but it is also found in many peripheral tissues, including the liver [38,39].

Collectively, the complex dynamic regulation of m^6A/m^6Am mRNA modifications controls mRNA transcription and translation, and dysregulation of this machinery is highly associated with several diseases, including different types of cancers [40]. In particular, initiation and/or progression of glioblastoma (GBM), acute myeloid leukemia (AML), breast cancer, pancreatic cancer, prostate cancer, cervical cancer, endometrial cancer, and HCC are affected by abnormal m^6A modifications or even by dysregulation of key players of the m^6A machinery [41–59]. In addition to the dysregulation of m^6A writers and readers, both m^6A erasers – FTO and ALKBH5 – have been linked to GBM, breast cancer, AML, cervical cancer, and HCC [40,41,43,60–65]. Knockdown of FTO in human HepG2 cells in mouse xenografts reduces tumor volume, suggesting that FTO may exert an oncogenic function in liver cancer via demethylation of *pyruvate kinase M2* (*PKM2*) mRNA [66]. Conversely, increased m^6A modifications and reduced *FTO* levels in human HCC samples compared to matched, non-tumor tissue have been reported [57,58]. Thus, the hepatocyte-specific function of FTO in HCC development remains elusive.

Here, we aimed to ascertain the role of FTO demethylase in DEN-induced HCC using mice with hepatic FTO deficiency. Liver-specific FTO inactivation increased DEN-induced HCC burden, potentially as a consequence of accelerated proliferation. Our findings demonstrate for the first time that hepatic FTO is dynamically regulated upon liver damage and has a protective role in HCC development *in vivo*.

2. MATERIAL AND METHODS

2.1. Animal care

Male mice (*Mus musculus*, genetic background C57Bl/6N) were housed in groups of 2–5 mice at 22–24 °C in a specific-pathogen-free animal facility and were exposed to a 12-h light/12-h dark cycle. The access to water and food was unlimited. Either control diet (Ssniff, EF D12450B* mod. LS) or normal chow diet (Ssniff, R/M-H low phytoestrogen) were fed. The experiments were authorized by the local government authorities and were in accordance with National Institutes of Health (NIH) guidelines.

2.2. Generation of FTO^{L-KO} mice

The $FTO^{fl/fl}$ mouse strain, in which loxP sites flank the exon 3 of the FTO gene, was obtained by EUCOMM and has been described previously [36]. Hepatocyte-specific FTO^{L-KO} mice have been generated by crossing the flp-deleted loxP-flanked FTO allele to $Alfp\text{-}Cre^{tg/wt}$. $FTO^{fl/fl}$ and FTO^{L-KO} mice were on a C57/BL6N background.

2.3. Glucose tolerance test

To analyze the reaction of mice to hyperglycemic stimuli, a glucose tolerance test was performed. Prior to the experiment, the mice were fasted. Fasted blood glucose was determined by punctuating the tail vain and using a Contour-Next® blood glucose meter and Contour-Next® test stripes. Next, mice were intraperitoneally (i.p.) injected with glucose (2 mg/g bodyweight (BW), Bela-Pharm, Vechta, Germany), and blood glucose levels were measured at 15, 30, 60, and 120 min after injection.

2.4. Insulin tolerance test

Insulin sensitivity was determined by performing an insulin tolerance test. Prior to the experiment, fed blood glucose levels were determined by punctuating the tail vain and using a Contour-Next® blood glucose meter and Contour-Next® test strips. Afterward, mice were injected i.p. with insulin (0.75 U insulin/g BW, Sanofi, Frankfurt, Germany), and blood glucose was measured at 15, 30, and 60 min after injection.

2.5. Long-term diethylnitrosamine (DEN)-induced HCC

At p15, male mice were injected i.p. with 25 mg/kg BW (2.5 mg/ml H_2O) DEN (Sigma–Aldrich, Seelze, Germany). The animals were sacrificed 8 months after DEN treatment, and tumor numbers were counted macroscopically.

2.6. Short-term DEN-induced acute liver damage

8-week-old mice were injected i.p. with 100 mg/kg BW DEN and sacrificed 4, 12, 24, and 48 h post-injection.

2.7. Organ preparation

Mice were sacrificed at the end of the experiment using a CO_2 chamber. First, epididymal white adipose tissue (WAT) and liver weights were determined. Heart blood was taken, and the liver, WAT, and skeletal muscle were snap-frozen in liquid nitrogen. The organs were stored at −80 °C until further analysis.

2.8. Nuclear magnetic resonance spectroscopy

Total fat and lean mass were measured using a minispec mq 7.5 (Bruker, Billerica, MA).

2.9. Adeno-associated-virus (AAV) injection

Prior to injection, 6-week-old mice were placed under an infrared lamp to ensure proper access to the tail vain. The mice were fixed in a restrainer, and 100 µl of virus in phosphate-buffered saline (PBS, 2.1×10^{13} genecopies/ml) was injected into the tail vain. AAVs were obtained from Vector Biolabs, Malvern, PA (shAAV-256372).

2.10. Cheek bleeding and serum analysis

Blood samples were collected from the submandibular vein using a lancet. Subsequently, blood was centrifuged for 60 min at 17,000 g at 4 °C, and serum was stored at -20 °C.

To monitor liver damage in the serum, alanine aminotransferase (ALT) levels were determined. Additionally, serum triglyceride and cholesterol levels were analyzed. The serum was analyzed by the central lab of the University Hospital in Cologne.

2.11. Enzyme-linked immunosorbent assay (ELISA)

Ki67 ELISA was performed to determine the amount of Ki67 in livers of ST-DEN-injected mice. The ELISA was performed as described by the manufacturer (Abbexa, Cambridge, UK, abx154289).

Ataxin-10 ELISA was performed to determine the amount of ataxin-10 in the serum of LT-DEN-injected mice at 6 and 8 months of age. The ELISA was performed according to the manufacturer's instructions (Uscn Life Science, Wuhan, CA). Mouse serum was diluted 1:10.

2.12. Western blot analysis

Tissue was homogenized with a bead homogenizer (MP Biomedicals, Irvine, CA) and lysed in radioimmunoprecipitation assay (RIPA) buffer (Cell Signaling, Denvers, MA) or triple lysate buffer for detection of CUL4A [67]. Protein concentrations were determined by Pierce BCA protein assay kit (ThermoScientific, Schwerte, Germany), Proteins were separated by sodium dodecyl sulfate —polyacrylamide gel electrophoresis (SDS-PAGE) and transferred to nitrocellulose or polyvinylidene difluoride (PVDF) membranes (Bio-Rad, Feldkirchen, Germany) using standard protocols. Membranes were probed with the following antibodies:

anti-β-ACTIN 1:5,000 (Sigma—Aldrich, Seelze, Germany, #A5441, RRID: AB_476744), anti-CCNE1 1:1,000 (Cell Signaling, Denvers, MA, #20808, RRID: AB_2783554), anti-Cleaved CASPASE3 1:200 (Cell Signaling, Denvers, MA, #9661, RRID: AB_2341188), anti- CUL4A 1:5,000 (Abcam, Cambridge, UK, #ab72548, RRID: AB_1268363), anti-FTO 1:5,000 [13], anti-PCNA 1:500 (Cell signaling, Denvers, MA, #13110, RRID: AB_2636979). Horseradish peroxidase (HRP)-conjugated secondary antibodies were used: polyclonal goat anti-mouse immunoglobulin G (IgG, whole molecule)-peroxidase (Sigma—Aldrich, Seelze, Germany, #A4416, RRID: AB_258167), polyclonal goat anti-rabbit IgG (whole molecule)-peroxidase (Sigma—Aldrich, Seelze, Germany, #A6154, RRID: AB_258284), polyclonal donkey anti-guinea pig IgG-peroxidase (Jackson Immuno Research, West Goove, PA, #706-035-148, RRID: AB_2340447).

ImageJ software was used for western blot quantification [68].

2.13. Quantitative polymerase chain reaction (PCR)

Frozen tissues or cells were homogenized in QIAzol (Qiagen, Hilden, Germany), and RNA was isolated using the RNeasy mini kit (Qiagen, Hilden, Germany) and treated with DNase (79254, Qiagen, Hilden, Germany). RNA was reversely transcribed with a High-Capacity cDNA Reverse Transcription Kit and amplified using TaqMan Gene Expression Master Mix (both Applied Biosystems, Darmstadt, Germany). Relative expression of mRNAs was determined using standard curves based on cDNA derived from the respective tissues, and samples were adjusted for total RNA content by TATA-binding protein (Tbp) quantitative PCR. Calculations were performed by a comparative cycle threshold (Ct) method: starting copy number of test samples was determined in comparison with the known copy number of the calibrator sample (ddCt). The relative gene copy number was calculated as 2-ddCt. Quantitative PCR was performed on an ABI Quantstudio Detector (Applied Biosystems, Darmstadt, Germany). The following TaqMan probes (Applied Biosystems, Darmstadt, Germany) were used for gene expression assays: *Cul4a* (Mm01220732_m1; Mm00461469_m1; Mm00461464_g1; Mm01220734_g1; Mm00461460_g1; Mm00461475_gH), *Dgat1* (Mm00515643_m1), *Dgat2* (Mm00499536_m1), *Fasn* (Mm00662319_m1), *Fto* (Mm00488755_m1), *Pparg* (Mm00440945_m1), *Scd1* (Mm00772290_m1), *Srebp1* (Mm00550338_m1), *Srebp2* (Mm01306292_m1), *Tbp* (Mm00446973_m1). Amplification of pronounced *Cul4a* methylation region in Exon 20 was performed using CAGAGACTATATGGAACGAGAC and ATCCTCTGCTCCGAATCCA primer and ACAGTCCAAATCAGTACCACTACGTGGC probe.

2.14. Quantitative proteomics

Fifty micrograms of isolated proteins were precipitated in ice-cold acetone overnight at -20 °C. Afterward, proteins were centrifuged 10 min at 15,000 *g* at 4 °C and washed once in 80% acetone (VWR, Darmstadt, Germany). Subsequently, protein pellets were dried at room temperature (RT) for 5 min and resuspended in 6 M of urea/2 M of thio-urea in 10 mM of HEPES (Applichem, Darmstadt, Germany). Prior to digestion, proteins were first reduced using 5 mM of TCEP for 1 h at RT and alkylated with 40 mM of CAA for 30 min. Protein digestion was performed by incubating for 3.5 h with Lys-C (1:100) (Wako, Neuss, Germany). Subsequently, the urea concentration was diluted to 2 M using 50 mM of ammonium bicarbonate and digested overnight at RT with trypsin (1:100) (Sigma—Aldrich, Seelze, Germany).

Prior to peptide loading, samples were acidified with 1:20 formic acid. StageTips were washed once with methanol (40 g for 1 min) (Roth, Karlsruhe, Germany), once with buffer B (80% acetonitril, 0.1% formic acid, Sigma—Aldrich, Seelze, Germany), and twice with buffer A (0.1% formic acid, Sigma—Aldrich, Seelze, Germany). Subsequently, peptides were loaded on StageTips and washed ones with Buffer A and twice with Buffer B. Dried StageTips were stored at 4 °C until elution and mass spectrometry analysis was performed [69].

Liquid chromatography tandem mass spectrometry (LC-MS/MS) instrumentation consisted of a nanoLC 1200 (ThermoScientific, Schwerte, Germany) coupled via a nano-electrospray ionization source to a QExactive HF-x mass spectrometer. Peptides were separated using an in-house packed (C18 PoroShell, 2.7 µm, Agilent, Santa Clara, CA) 50-cm column (ID: 75 µm) and a binary buffer system: A) 0.1% formic acid and B) 0.1% formic acid in 80% acetonitrile. In total, a gradient of 90 min was used with a linear increase from 4% B to 32% B within 75 min, followed by an increase to 95% B and re-equilibration steps.

MS1 spectra were acquired at a mass resolution of 60,000 using an AGC target of 3e6 and a maximum injection time of 20 ms. The mass spectrometer operated in a Top18 data-dependent mode using an MS/MS mass resolution of 7,500 (at 200 *m/z*), a maximum injection time of 11 ms (AGC target 1e5). The isolation window was set to 1.3 *m/z*. A normalized collision energy of 28 was used.

Acquired MS/MS spectra were correlated against the Uniprot Mus Musculus reference proteome (downloaded Jan. 2019) using MaxQuant [70] and the search engine Andromeda [71]. MaxQuant settings were used as default and match-between runs and the MaxLFQ algorithm were enabled. To identify significantly changed proteins, a two-sided t-test was performed. Visualization and analysis of data were performed in Instant Clue [72].
The mass spectrometry proteomics data have been deposited to the ProteomeXchange Consortium via the PRIDE [73] partner repository with the dataset identifier PXD018223.

2.15. Methyl-RNA-immunoprecipitation (meRIP)

To isolate mRNA from liver lysates, a magnetic mRNA isolation kit (NEB, Frankfurt am Main, Germany) was used. The isolation was performed as described by the manufacturer. The mRNA concentration was determined using a NanoDrop ND-1000 UV-Vis Spectrophotometer. Two micrograms of mRNA was denaturated at 94 °C for 4 min. Ten milligrams of anti-N6-methyladenosine or control mouse immunoglobulin G (IgG) antibody in 450 μl of CLIP buffer (50 mM of Tris-HCl, pH 7.4, Applichem, Darmstadt, Germany, 150 mM of NaCl, Applichem, Darmstadt, Germany, 0.5% NP40, Sigma—Aldrich, Seelze, Germany) containing 2 μl of RNaseOUT (ThermoScientific, Schwerte, Germany) and 0.9 μl of Ethylenediaminetetraacetic acid EDTA (Applichem, Darmstadt, Germany) was added to the mRNA and incubated on a rotor for 1 h at RT. In the meantime, 1.5 mg of Protein A beads (ThermoScientific, Schwerte, Germany) were washed in CLIP buffer and subsequently resuspended in 100 μl of CILP buffer. After antibody binding, 100 μl of Protein A beads in CLIP buffer were added to the mRNA, and IP was performed on a rotor overnight at 4 °C. Subsequently, IP was washed 3 times in 500 μl of high-salt CLIP buffer (50 mM of Tris-HCl, pH 7.4, 1 M of NaCl, 0.5% NP40), followed by 3 washes in CLIP buffer. To elute immunoprecipitated RNA, the beads were resuspended in 300 μl of elution buffer (5 mM of Tis-HCl pH 7.5, 1 mM of EDTA, 0.05% SDS, Applichem, Darmstadt, Germany) containing 5 μl of Proteinase K (Roche Diagnostics, Mannheim, Germany) and incubated for 1.5 h at 37 °C while shaking gently. Immunoprecipitated mRNA was purified by phenol/chloroform extraction. To this end, 300 μl of 1:1 phenol/chloroform (Roth, Karlsruhe, Germany) were added to eluted mRNA and vortexed thoroughly. Subsequently, mRNA was centrifuged for 10 min at 17,000 g at 4 °C. mRNA containing upper phase was mixed with 600 μl of 100% ethanol (Applichem, Darmstadt, Germany). After centrifugation, mRNA was washed in 70% ethanol and dried for 10 min at 37 °C. The purified mRNA was resuspended in 20 μl of diethyl pyrocarbonate (DEPC, Applichem, Darmstadt, Germany) water, and concentration was determined using a NanoDrop ND-1000 UV-Vis Spectrophotometer. Subsequently, mRNA was reversely transcribed into cDNA and quantitative reverse transcription polymerase chain reaction (qRT-PCR) was performed.

2.16. SELECT assay

The select assay was performed as previously described by Xiao et al. [74]. In brief, polyA mRNA or RNA oligos (IDT) were mixed with 40 nM of the respective UP and DOWN primer (listed below) and 5 μM of dTTPs in 17 μl 1x CutSmart buffer (NEB). Annealing was performed at a temperature gradient (1 min at 90 °C, 1 min at 80 °C, 1 min at 70 °C, 1 min at 60 °C, 1 min at 50 °C, and 6 min at 40 °C). Three microliters of Bst 2.0 (NEB) and SplintR (NEB) enzyme mixture (0,01 U Bst 2.0 DNA polymerase, 0,5 U SplintR ligase, 10 nmol ATP) were added and incubated for 20 min at 40 °C. Subsequently, denaturation was performed at 80 °C for 20 min. qRT-PCR was performed on an ABI Quantstudio Detector (Applied Biosystems, Darmstadt, Germany). The 20 μl reaction contained 2x SYBR Select Mastermix (Applied Biosystems), 200 nM of qPCRF and 200 nM qPCRR primer, 2 μl of SELECT reaction and ddH_2O. qRT-PCR was run using the following conditions: 1: 5 min at 95 °C; 2: 10 s at 95 °C, 35 s at 60 °C x 40 cycles; 3: 15 s at 95 °C; 4: 1 min at 60 °C; 5: 15 s at 95 °C (ramping rate 0,05 °C/s); 6: hold 4 °C.
Primers used for SELECT:
Cul4m6A2373up: tagccagtaccgtagtgcgtgTTTGGACTGTCTTTGTCTCG
Cul4m6A2373down: 5P- TCCATATAGTCTCTGTCTATAcagaggctgag tcgctgcat
Cul4m6A2378up: tagccagtaccgtagtgcgtgACTGATTTGGACTGTCTTTG
Cul4m6A2378down: 5P- CTCGTTCCATATAGTCTCTGcagaggctgagtc gctgcat
Cul4m6A2384up: tagccagtaccgtagtgcgtgGTGGTACTGATTTGGACTG
Cul4m6A2384down: 5P- CTTTGTCTCGTTCCATATAGcagaggctgagtc gctgcat
Cul4m6A2415up: tagccagtaccgtagtgcgtgGACAGTCAGCTGGTGCG
Cul4m6A2415down: 5P- CATGCCACGTAGTGGTACcagaggctgagtcg ctgcat
Cul4m6A2427up: tagccagtaccgtagtgcgtgCTCACTGGGAGACGACAG
Cul4m6A2427down: 5P- CAGCTGGTGCGTCATGCcagaggctgagtc gctgcat
Cul4A2381up: tagccagtaccgtagtgcgtgGGTACTGATTTGGACTGTCT
Cul4A2381down: 5P- TGTCTCGTTCCATATAGTCTcagaggctgagtc gctgcat
Cul4A2412up: tagccagtaccgtagtgcgtgCAGTCAGCTGGTGCGTCA
Cul4A2412down: 5P- GCCACGTAGTGGTACTGAcagaggctgagtcgctgcat
Cul4A2391up: tagccagtaccgtagtgcgtgCCACGTAGTGGTACTGATT
Cul4A2391down: 5P- GGACTGTCTTTGTCTCGTTcagaggctgagtcgctgcat
RNA oligos:
m6A2415:AUCAGUACCACUACGUGGCAUG**iN6MerA**CGCACCAGCUG ACUGUCGUCU
A2415: AUCAGUACCACUACGUGGCAUG**A**CGCACCAGCUGACUGUCGUCU
qPCRF for SELECT: ATGCAGCGACTCAGCCTCTG
qPCRR for SELECT: TAGCCAGTACCGTAGTGCGTG

2.17. Immunohistochemistry and histological analysis

Liver tissue was embedded in tissue-freezing medium (Jung, Heidelberg, Germany) for frozen block preparation. To detect proliferating cells, Ki67 (#ab 15580, Abcam, Cambridge, UK) staining was performed on cryosections of livers. Ki67-positive cells were imaged using a Zeiss Imager fluorescence microscope. The number of Ki67-positive cells was normalized to the total number of cells (4′,6-diamidino-2-phenylindole (DAPI)-positive) using ImageJ [68]. Oil-Red-O (Sigma—Aldrich, Seelze, Germany, O0625-25G) staining was performed to visualize hepatic lipid storage. Cryosections of livers were fixed in formalin and subsequently washed in tap water for 10 min. Next, liver sections were rinsed with 60% isopropanol (Roth, Karlsruhe, Germany) and stained for 15 min with Oil red O working solution. After rinsing with 60% isopropanol, hematoxylin and eosin staining was performed to visualize nuclei and cytoplasm, respectively.

2.18. Indirect calorimetry

Energy expenditure was measured using indirect calorimetric measurements in a PhenoMaster System (TSE systems, Bad Homburg, Germany). Animals were allowed to adapt to the single housing in metabolic chambers for a training phase of 5 days. During that time, animals were monitored daily to ensure proper adaptation to the drinking and feeding dispensers. Calorimetric measurement was conducted at 22—24 °C over a period of 48—72 h, assessing oxygen

consumption (VO_2), carbon dioxide production (VCO_2), locomotor activity by interruption of a light beam (light barrier frame, TSE systems, Bad Homburg, Germany), and water and food intake using automated measuring devices (TSE systems, Bad Homburg, Germany) for individually housed mice. Energy expenditure and the respiratory exchange ratio (VCO_2/VO_2) were calculated indirectly from the obtained parameters.

2.19. Quantification and statistical analysis

Data are presented as means ± min. and max. or means ± SEM. Statistical significance was either calculated using a two-tailed unpaired student's t-test, ordinary one-way analysis of variance (ANOVA), or ordinary two-way ANOVA. Significance was accepted at the level of $p^* \leq 0.05$, $p^{**} \leq 0.01$, $p^{***} \leq 0.001$, and $p^{****} \leq 0.0001$. The respective statistical test that was used is indicated in each figure legend. ImageJ was used for microscopy and Western blot quantification [68]. Visualization and analysis of proteomics data was done in InstantClue [72]. Bar charts and columns were generated in PRISM. Figures were assembled with Adobe Illustrator.

3. RESULTS

3.1. Hepatic FTO deficiency alters body composition in late stage DEN-induced HCC but fails to impact glucose metabolism

To specifically determine the function of hepatic FTO in HCC development, we generated mice with hepatocyte-specific ablation of FTO. $Fto^{tm1c(EUCOMM)Wtsi}$ mice were intercrossed with Alfp-Cre mice [75] to remove the loxP flanked exon 3 of the *Fto* gene specifically in hepatocytes (Supplementary Figure 1A). $FTO^{fl/fl}$; Alfp-Cre^{tg} (FTO^{L-KO}) mice showed reduced *Fto* mRNA and FTO protein levels in liver lysates when compared to $FTO^{fl/fl}$ (Ctrl) mice (Supplementary Figures 1B and C). Of note, the $Fto^{tm1c(EUCOMM)Wtsi}$ allele, neither in the loxP-flanked nor in the Cre-mediated deleted state, affects the SNP region in intron 1 of FTO that has been identified in human GWAS studies associated with increased body mass index.

Whole body FTO deficiency protects against obesity due to increased energy expenditure, while whole body FTO overexpression leads to an increase in body and fat mass, as well as to glucose intolerance upon high-fat diet feeding [13,14]. To date, liver FTO function has not been investigated in a genetic mouse model of hepatocyte-specific FTO depletion. Therefore, we set out to metabolically analyze FTO^{L-KO} mice and their littermate Ctrls. First, body weight was monitored weekly over a period of 18 weeks. However, FTO^{L-KO} mice did not show changes in body weight when compared to Ctrl mice (Supplementary Figure 1D). Consistently, no difference was detected in fat mass and epididymal white adipose tissue (WAT) weight in 18-week-old Ctrl and FTO^{L-KO} mice (Supplementary Figures 1E and F). Moreover, hepatic depletion of FTO did not change total liver weights (Supplementary Figure 1G). Given the mild improvement in insulin sensitivity of FTO whole body knockouts and the reduction of glucose tolerance in FTO overexpressing mice, we assessed insulin sensitivity and glucose tolerance in Ctrl and FTO^{L-KO} mice (Supplementary Figures 1H and I) [13,14]. However, no difference was observed in either insulin sensitivity (Supplementary Figure 1H) or glucose tolerance (Supplementary Figure 1I) at 13 weeks of age. Blood glucose levels in fed and fasted states remained unchanged in Ctrl and FTO^{L-KO} mice (Supplementary Figure 1J). Furthermore, we investigated food intake, activity, respiratory exchange ratio, and energy expenditure (Supplementary Figure 1K, L, M, and N). We found that hepatic depletion of FTO did not change any of those parameters. Thus, hepatic FTO fails to affect whole body energy metabolism, activity, and food intake.

Based on the impact of m^6A methylation in cancer initiation and progression, we aimed to define the role of hepatic FTO in chemically-induced HCC development. To ensure that HCC development is independent of metabolic changes in DEN-injected mice, we monitored body composition and glucose metabolism as part of the 8-month DEN protocol (Figure 1A). Although bodyweight gain was similar between the groups throughout the experiment, FTO^{L-KO} mice showed a significant reduction in body weight after 8 months of age (Figure 1B,C). Fat mass and epididymal WAT weight was reduced in mice with hepatic FTO deficiency upon DEN treatment (Figure 1D,E). However, overall insulin sensitivity and glucose tolerance remained largely unaffected in FTO^{L-KO} mice at early (3 months) and late time points (6 months) of DEN-induced liver carcinogenesis (Figure 1F,G). Consistently, no differences in blood glucose levels were observed upon hepatic FTO depletion in fed and fasted states (Figure 1H). Recent studies have shown that FTO overexpression in HepG2 and L02 cells increased lipid accumulation [76,77]. Moreover, NASH patients and NASH animal models displayed increased hepatic FTO expression [76,78]. However, Oil-Red-O staining of livers from DEN-injected FTO^{L-KO} and Ctrl mice did not display differences in lipid accumulation between the genotypes (Figure 1I). Hepatic FTO deficiency might have an impact on metabolic pathways, such as cholesterol homeostasis, triglyceride and fatty acid synthesis, and glycolysis/glycogenesis. However, expression of the key cholesterol homeostasis regulatory genes *Srebp1* and *Srepb2* as well as serum cholesterol levels remained unchanged in FTO^{L-KO} mice compared to their littermate Ctrl mice (Supplementary Figure 2A). Additionally, expression of central enzymes of triglyceride synthesis *Dgat1* and *Dgat2* were unaltered in livers of mice with FTO deficiency (Supplementary Figure 2B). In line, serum triglyceride levels did not differ between the genotypes (Supplementary Figure 2B). Moreover, other lipid metabolism regulatory genes, such as *Scd1*, *Pprg*, and *Fasn,* were similarly expressed in livers of both genotypes (Supplementary Figure 2C). Such enzymes in the liver have also been shown to be dysregulated in cancer-induced cachexia [79]. To prove whether decreased body weight is caused by elevated cachexia in the FTO^{L-KO} mice, we investigated serum levels of ATAXIN-10, shown to be a potent marker for cancer cachexia [80], in serum of 6 and 8 months-old Ctrl and FTO^{L-KO} mice (Supplementary Figure 2D). However, ATAXIN-10 serum levels were unchanged in both cohorts at 6- and 8-month time points of liver carcinogenesis, indicating that Ctrl and FTO^{L-KO} mice suffered similarly if at all from cachexia.

Taken together, these results ensure that DEN-induced HCC development in Ctrl and FTO^{L-KO} cohorts occurred in the absence of large metabolic alterations allowing for the direct comparison between the genotypes independent of an altered metabolism.

3.2. Hepatic FTO expression counteracts DEN-induced HCC development

To monitor DEN-induced HCC progression indirectly via assessing marker of liver damage, we measured alanine aminotransferase (ALT) activity in the serum of 6- and 8-month-old mice. While after 6 months of age, serum ALT activitiy was low in Ctrl and FTO^{L-KO} mice, indicating no or little HCC-associated liver damage, liver damage tended to increase in both genotypes after 8 months (Supplementary Figure 3A). However, no significant differences were obtained between the two genotypes. At 8 months of age, the mice were sacrificed and analyzed for tumor burden. We found that the liver weight of FTO^{L-KO} mice was slightly increased when compared to Ctrl animals (Supplementary Figure 3B). In addition, the amount of Ki67-positive cells was slightly elevated, which points toward increased proliferation in livers of

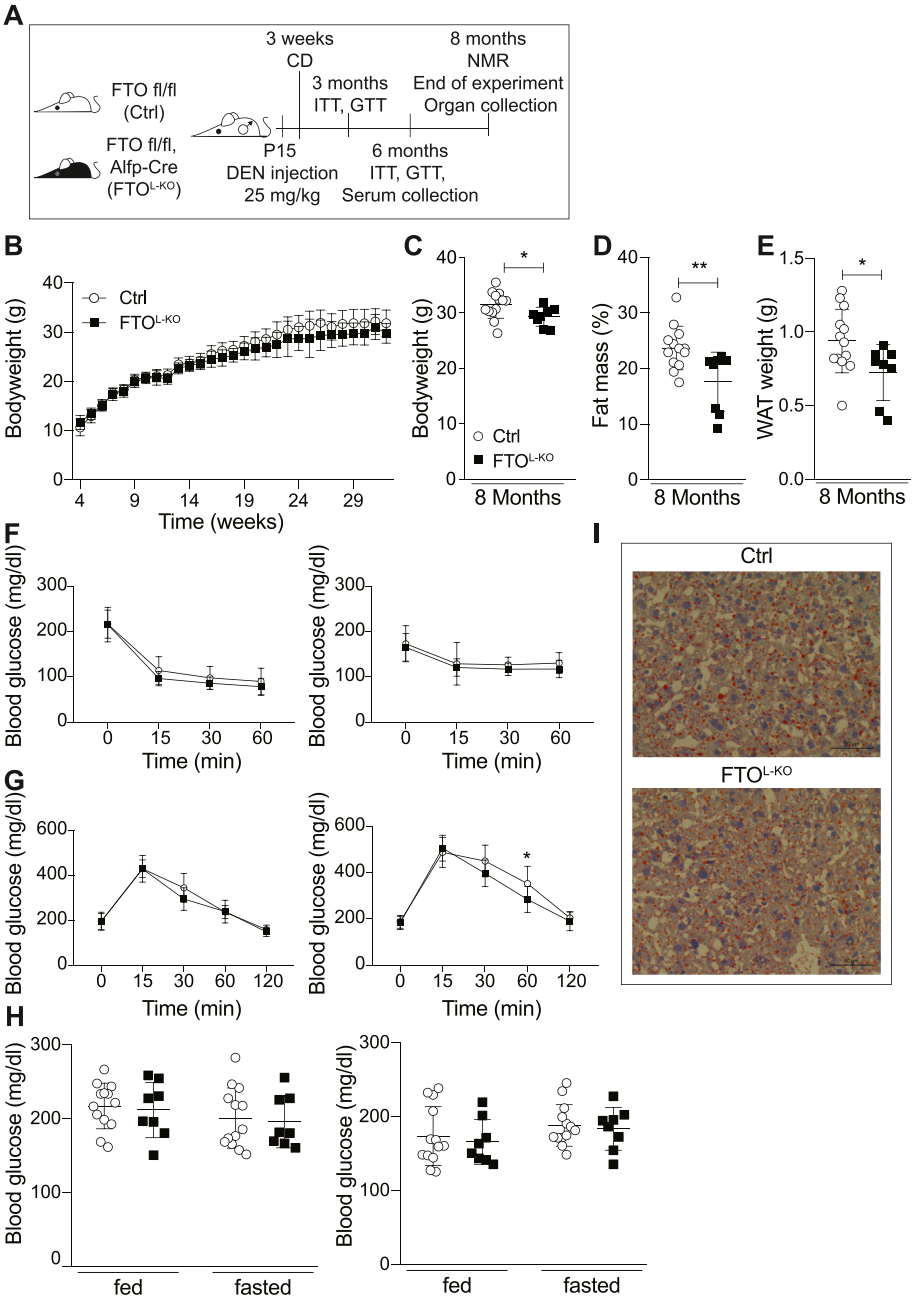

Figure 1: Hepatic FTO deficiency reduces fat mass and body weight but does not alter glucose metabolism in DEN-injected mice. (A) Timeline of DEN-induced hepatocellular carcinoma experiments. CD = control diet, ITT = insulin tolerance test, GTT = glucose tolerance test, NMR = nuclear magnetic resonance spectroscopy, DEN = diethylnitrosamine. (B) Body weight curve of Ctrl and FTO^{L-KO} mice (n = 8–13). (C) Body weight of Ctrl and FTO^{L-KO} mice at 8 months of age (n = 8–13, two-tailed unpaired t-test). (D) Fat mass of Ctrl and FTO^{L-KO} mice at 8 months of age (n = 8–13, two-tailed unpaired t-test). (E) Absolute epididymal WAT weight of Ctrl and FTO^{L-KO} mice at 8 months of age (n = 8–13, two-tailed unpaired t-test). (F) Insulin tolerance determined at 11 (left) and 24 (right) weeks of age of Ctrl and FTO^{L-KO} mice (n = 7–13, two-way ANOVA). (G) Glucose tolerance determined at 12 (left) and 25 (right) weeks of age of Ctrl and FTO^{L-KO} mice (n = 8–12, two-way ANOVA). (H) Blood glucose levels determined after 3 (left) and 6 (right) month of age of Ctrl and FTO^{L-KO} mice. Mice were either fed *ad libitum* or fasted (n = 8–13, two-way ANOVA). (I) Representative pictures of liver Oil red O stainings from Ctrl and FTO^{L-KO} mice at 8 months of age (n = 4–8). Scale bar = 50 μm p* 0.05, p** 0.01. Data are means with SD.

FTO^{L-KO} mice (Supplementary Figure 3C). In contrast, no changes in PCNA levels of liver lysates were detected in FTO^{L-KO} mice (Supplementary Figure 3D). To examine potential differences in apoptosis among the genotypes, cleaved CASPASE3 levels of liver lysates of 8-month-old mice were determined, but no changes were detected (Supplementary Figure 3D).

However, hepatic FTO deficiency resulted in an increased HCC burden from approximately 8 tumors in Ctrl animals to 15 in the FTO-deficient livers on average (Figure 2A). When we analyzed tumor sizes macroscopically, not only the amount of small sized (<2 mm) tumors was increased significantly in FTO^{L-KO} mice, but also the amount of large sized (>2 mm) tumors was 2.6-fold elevated in livers of FTO-

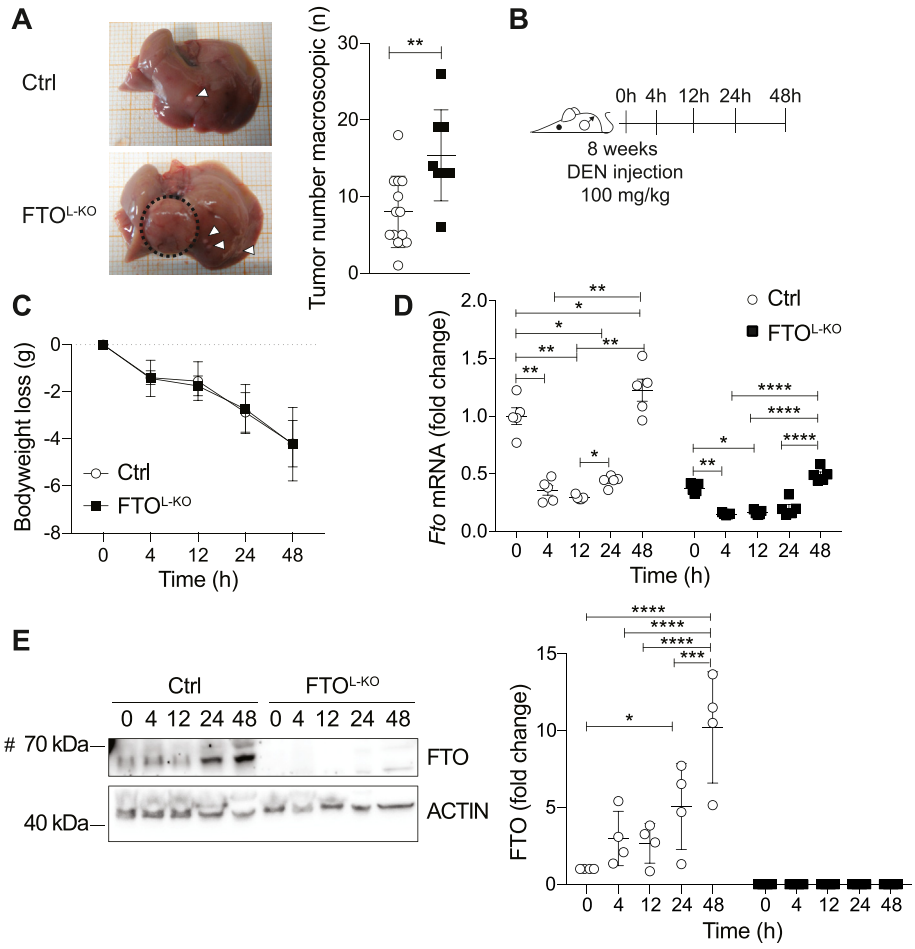

Figure 2: FTO protects against HCC development and progression and acute liver damage induced by short-term-DEN injection increases hepatic FTO expression over time. (A) Tumor number after 8 months of age of Ctrl and FTO^{L-KO} mice (n = 8–13, two-tailed unpaired t-test). (B) Time beam of ST-DEN experiments and respective timepoints. DEN injection at 8 weeks of age. DEN = diethylnitrosamine. (C) Bodyweight loss at different ST-DEN timepoints (n = 5 for each timepoint, two-way ANOVA). (D) qPCR analysis of *Fto* expression in whole liver of ST-DEN injected Ctrl and FTO^{L-KO} mice (n = 5 for each timepoint, two-way ANOVA). (E) Western blot analyses of FTO in whole liver lysates isolated from ST-DEN injected Ctrl and FTO^{L-KO} mice (representative blot) and respective quantification (n = 4 for each timepoint, two-way ANOVA). FTO/β-ACTIN ratio normalized to 0 h Ctrl expression. # = unspecific band. p* 0.05, p** 0.01, p*** 0.0002, p**** 0.0001. Data are means with SD.

deficient mice (Supplementary Figure 3E). This indicates that FTO deficiency not only impacts HCC initiation (increased tumor numbers) but also HCC progression (increased numbers of larger tumors). Collectively, our experiments reveal that hepatic FTO function plays a protective role in the development of HCC *in vivo*.

Given the protective effect of hepatic FTO expression in HCC development and the lack of significant changes in proliferation and cell death at late time points, we hypothesized that alterations in the tumor inititation phase might cause increased tumor numbers in FTO-deficient livers after long-term DEN injection. Thus, we investigated the role of FTO in the tumor initiation phase. Therefore, 8-week-old Ctrl and FTO^{L-KO} mice were injected with a sublethal dose (100 mg/kg) of short-term DEN (ST-DEN) to induce acute liver damage and sacrificed 4 h, 12 h, 24 h, and 48 h after injection, respectively (Figure 2B). Moreover, we analyzed a non-injected control group, referred to as 0 h. Body weight loss of the mice was monitored and decreased significantly over time in both Ctrl and FTO^{L-KO} mice to the same extent (Figure 2C). We found that *Fto* mRNA as well as FTO protein levels were dynamically regulated in the livers of Ctrl mice (Figure 2D,E). In detail, FTO levels were 5- to 10-fold increased 24 h and 48 h post-DEN-injection, respectively (Figure 2E). Thus, these results suggest an important role for FTO in hepatic regeneration after chemically-induced liver damage as well as in the tumor initiation phase of HCC.

3.3. *Cul4a* mRNA is a downstream target of FTO upon acute liver damage

The protective effects of hepatic FTO expression on HCC initiation might be direct, e.g., via demethylation of RNAs encoding proteins involved in tumorigenesis or indirect e.g., via targets that alter global translation or transcription. To determine candidates of damage-induced liver carcinogenesis in the absence of FTO without dependence on anti m^{6}A/m^{6}Am antibody-mediated pull-down of RNA, we performed mass spectrometry-based proteomics analysis of liver lysates isolated from Ctrl and FTO^{L-KO} mice at 0 h, 12 h, and 24 h upon ST-DEN injection. Thus, this strategy should allow for finding candidate proteins that are affected by FTO deficiency and are potentially causative for increased tumor burden in the long-term DEN-injected HCC model. We aimed for the identification of temporally regulated proteins in response to ST-DEN injections. Among other interesting candidates (listed in Supplementary Table 1), the protein CUL4A caught

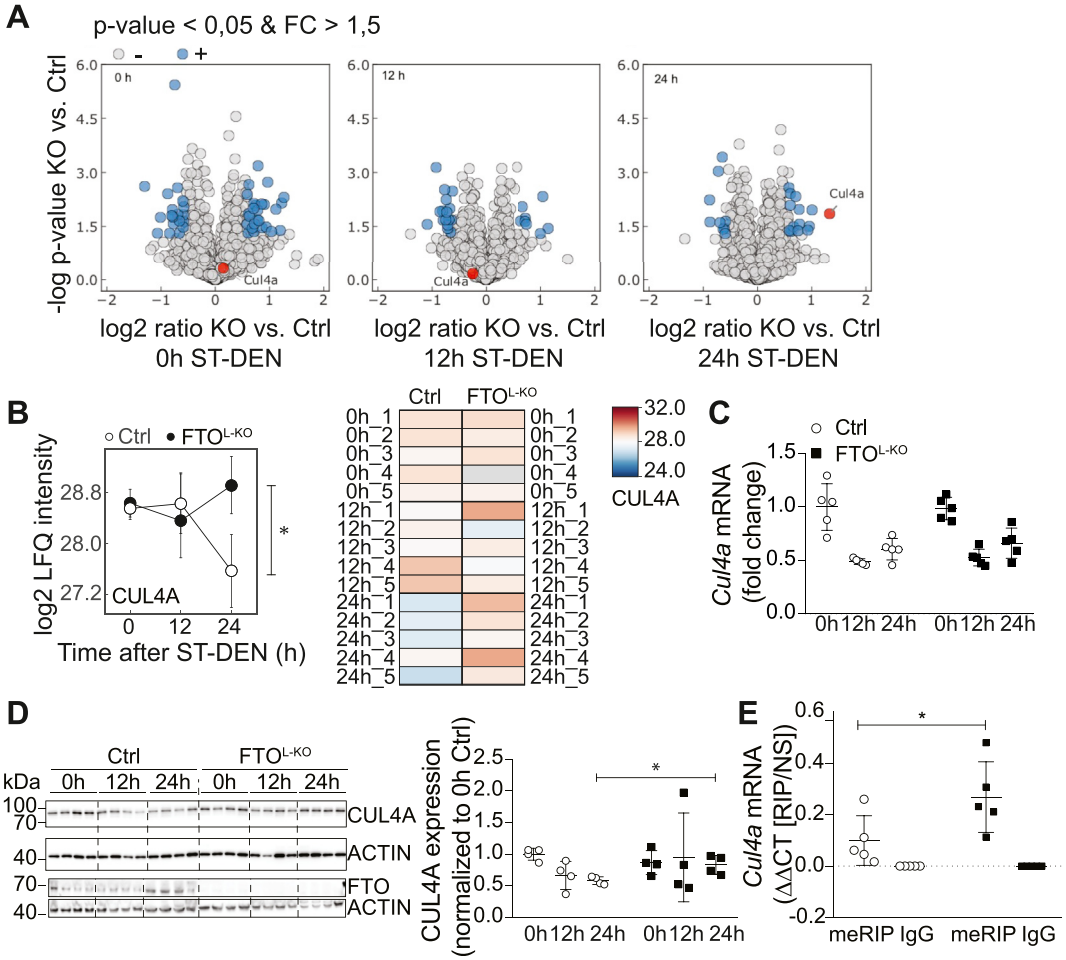

Figure 3: Hepatic FTO negatively regulates CUL4A in response to short-term DEN-induced liver damage. (A) Volcano plot of log2 ratio of livers of Ctrl and FTO^{L-KO} at 0h, 12h, and 24h after ST-DEN injection vs the −log10 p value of a two-sided t-test (blue = significantly changed proteins (abs. log2 fold change >0.58 and p-value < 0.05), red = CUL4A). (B) Log2 LFQ intensities of CUL4A in Ctrl and FTO^{L-KO} liver lysates at 0 h, 12 h, and 24 h after ST-DEN injection. (C) qPCR analysis of *Cul4a* expression in whole liver of ST-DEN injected Ctrl and FTO^{L-KO} mice (n = 5 for each timepoint, two-way ANOVA). (D) Western blot analyses of CUL4A and FTO in whole liver lysates isolated from ST-DEN injected Ctrl and FTO^{L-KO} mice and respective quantification (n = 4 for each timepoint, two-tailed unpaired multiple t-tests). CUL4A/β-ACTIN ratio normalized to 0 h Ctrl expression. (E) Methyl-RNA immunoprecipitation and IGG ctrl immunoprecipitation and subsequent qRT-PCR analysis of *Cul4a* mRNA pulldown in mRNA isolated from livers of 24 h ST-DEN injected Ctrl and FTO^{L-KO} mice (n = 5, two-way ANOVA). p* 0.05. Data are means with SD (B–E) or SEM (H).

our attention because the expression remained at high levels in FTO-deficient livers, whereas in Ctrl livers CUL4A was significantly reduced 24 h after ST-DEN injection (Figure 3A,B). This regulation was confirmed via Western blot analysis; however, mRNA levels of *Cul4a* did not reflect the same regulation as CUL4A protein, i.e., mRNA expression decreased upon liver damage but independent of FTO, which suggests a post-transcriptional rather than a transcriptional regulation of *Cul4a* (Figure 3C,D). Given that CUL4A protein expression reversely correlated with FTO expression in Ctrl livers, we hypothesized that *Cul4a* might be a potential downstream target of FTO. To test this hypothesis, we took advantage of a publicly available RNA sequencing dataset [81]. Zhou et al. performed methyl-RNA-immunoprecipitation (meRIP) with subsequent RNA sequencing of livers from Ctrl and FTO overexpressing (FTO-OE) mice. We analyzed m^{6}A modification levels of the *Cul4a* mRNA in the liver of FTO-OE compared to Ctrl mice and identified that *Cul4a* mRNA is hypomethylated in the FTO-OE mouse in the region between 118 and 183 bp encoded by exon 1 and the most prominent peak at 2340–2427 bp surrounding the translational STOP codon in exon 20 (Supplementary Figures 3F and G). These data supported the hypothesis that *Cul4a* mRNA might be a downstream target of FTO. To further validate these results in our FTO^{L-KO} mice, we conducted meRIP on fragmented mRNA isolated from the livers of 24 h ST-DEN injected Ctrl and FTO^{L-KO} mice and subsequently performed qRT-PCR analysis using probes against exons with potential methylation sites, e.g., exons 1/2 and exon 20 as well as in other regions, such as exons 2/3 and 17/18 of the *Cul4a* transcript (Figure 3E, Supplementary Figure 3H). However, while qRT-PCR with most probes revealed increased appearance of mRNA derived from FTO-deficient livers, only the fragment of exon 20 was significantly enriched in the livers of FTO^{L-KO} mice (Figure 3E, Supplementary Figure 3H). Notably, direct examination of *Cul4a* mRNA levels by qRT-PCR without meRIP in livers of Ctrl and FTO^{L-KO} mice did not show different mRNA abundances with all probes used (Supplementary Figure 3I). Subsequently, we focused on the region 2359–2427 of the *Cul4a* transcript of exon 20, which showed the highest methylation differences in the FTO-OE vs. Ctrl liver, and that additionally represents the region of qRT-PCR probe exon 20 in the meRIP (Figure 3E). In this region, all adenosines within a potential m^{6}A

consensus sequence [82] were considered as potential FTO target adenosines (red), whereas 3 adenosines without consensus sequence were used as controls (Supplementary Figure 4A green). Subsequently, the single-base elongation- and ligation-based qRT-PCR amplification method (SELECT) [74] was performed, which does not depend on use of an anti m^6A/m^6Am antibody, to identify potential target sites of FTO in *Cul4a* mRNA of livers isolated from 24 h ST-DEN treated FTO^{L-KO} and Ctrl mice. Of note, the SELECT method was suitable for determination of m^6A modifications in synthetic RNA oligos and the authors used recombinant FTO to assist their detection model, but the *in vivo* validation was missing. The SELECT method takes advantage of the fact that m^6A-modified RNA hinders the single base elongation of Bst DNA polymerase and nick ligation efficiency of SplintR ligase. Two synthetic DNA oligos fused to PCR adapters (up and down probe) anneal to mRNA but leave a nucleotide gap opposite to an m^6A site (Supplementary Figure 4B). SELECT results revealed that only adenosine 2415, which is the A of the STOP codon UGA of *Cul4a* transcript, showed significantly higher CT cycles in FTO^{L-KO} livers compared to Ctrl livers, suggesting that this specific site was hypermethylated in the FTO^{L-KO} livers upon ST-DEN treatment (Supplementary Figure 4C). In contrast, not only control As 2381, 2391, and 2412 remained unchanged across the genotypes, but the remaining potential m^6A sites 2373, 2378, 2384, and 2427 did not show a difference in CT values, indicating that those sites are not targeted by FTO demethylase *in vivo* (Supplementary Figures 4D and E). To estimate how much of *Cul4a* 2415A is methylated in FTO-deficient livers, upon liver damage, we synthesized 44 bp synthetic RNAs 2415A and 2415m^6A homologous from 2392 to 2436 flanking the 2415 region to be used in SELECT assay in serial dilutions ranging from 50 to 0.15625 nM (Supplementary Figures 4F–I). These analyses revealed that RNA 2415m^6A came up later in the qRT-PCR cycle than 2415A at all concentrations (in average 2.9 cycles later, Supplementary Figure 4I). FTO^{L-KO} RNA appeared 2.7 cycles later than Ctrl RNA when using 2415 oligos in SELECT, which suggests that approximately 95% of 2415A is methylated in FTO-deficient *Cul4a* mRNA upon acute liver damage. Taken together, these results suggest *Cul4a* mRNA as a target of increased FTO levels upon 24 h ST-DEN-induced liver damage. Consequently, this might alter *Cul4a* translation in FTO-deficient livers in 24 h ST-DEN, which we have identified by the proteomics approach. However, our experimental set-up does not provide ultimate proof that *Cul4a* mRNA is demethylated by FTO; thus, alternative conclusions might be drawn regarding how FTO regulates CUL4A protein abundance upon acute liver damage.

3.4. Knockdown of CUL4A *in vivo* rescues elevated proliferation upon chemically-induced acute liver damage in FTO^{L-KO} mice

CUL4A is a member of the CULLIN family, which consists of proteins that are part of E3 ubiquitin ligase complexes [83]. Previous findings have shown that CUL4A regulates processes such as cell cycle progression, DNA replication, genomic stability, hematopoiesis, and spermatogenesis [83]. Increased CUL4A expression has been linked to several cancers, including HCC [84,85]. CUL4A was shown to regulate CDK inhibitors and cyclin E1 in *Drosophila,* resulting in S phase entry, thereby driving cell cycle progression [86]. Western blot analysis revealed that CYCLIN E1 (CCNE1) remained stable in livers of FTO^{L-KO} mice upon chemically-induced liver damage (Figure 4A), whereas in Ctrl livers, CCNE1 expression was dynamically regulated after ST-DEN-injection (Figure 4A). The elevated expression levels of CCNE1 in FTO-deficient livers proposed an enhanced G1 to S phase entry and thus elevated proliferation in those livers. Our results suggest that elevated translation of *Cul4a* in livers of FTO^{L-KO} mice may result in enhanced cell cycle progression and proliferation, ultimately contributing to an increased development of HCC.

As CUL4A promotes cell cycle progression and proliferation, we hypothesized that reducing CUL4A expression in FTO^{L-KO} mice can protect these animals from an exaggerated DEN-response. Thus, we knocked down CUL4A *in vivo* in Ctrl and FTO^{L-KO} mice (Figure 4B). Tail vein injection of an AAV-expressing shRNA, which targets *Cul4a*, resulted in significantly reduced *Cul4a* mRNA and CUL4A protein levels in single- and double-deficient livers, but not in mice injected with an AAV-expressing a scrambled control shRNA (*scrmbl* Ctrls) (Figure 4C,D). Hepatocyte-specific depletion of *Fto* mRNA and FTO protein was confirmed via qRT-PCR and Western blot analysis (Figure 4C,D). To investigate the proliferation in the livers of these mice at 24 h after ST-DEN injections, a Ki67 ELISA was performed (Figure 4E). Indeed, knockdown of *Cul4a* resulted in a significant reduction of total Ki67 levels in the liver of double-deficient animals when compared to the FTO^{L-KO} mice. Of note, Ki67 levels in double-deficient livers were completely restored when compared to Ki67 levels in *Cul4a* single knockdown animals. Thus, reduction of CUL4A expression was sufficient to rescue the elevated proliferation in the livers of FTO^{L-KO} mice. Collectively, these results suggest that elevated FTO levels during acute liver damage inhibited *Cul4a* translation, which consequently resulted in reduced proliferation and thus, in reduced HCC burden *in vivo*.

4. DISCUSSION

FTO whole body deficiency in mice results in metabolic alterations characterized by a lean phenotype due to increased energy expenditure and growth retardation, whereas the overexpression of FTO manifests an opposing phenotype, which is accompanied by an elevated susceptibility to obesity caused by an increase in food intake [13,14,87,88]. However, the extent to which the FTO gene itself contributes to metabolic alterations in human high-risk SNP carriers remains unclear. These SNPs are located within a region of the first intron of the human *FTO* gene and are one of the strongest known genetic factors associated with human obesity [10,11]. Previous studies have shown that the intronic region harboring high-risk SNPs affect the regulation and expression of distal genes, such as *IRX3* and *RPGRIP1L* [15–18]. In consistency, disruption of *Irx3* in mice results in a reduction of body weight up to 30% [15], whereas hypomorphic *Rpgrip1l* mice display a diminished leptin responsiveness and are hyperphagic and obese [18]. Thus, human predisposition to obesity of at-risk carriers within the *FTO* gene may indicate a rather indirect than a direct role for FTO. However, mouse models of FTO deficiency, which do not affect the intronic region of the at-risk SNPs, as well as over expression display metabolic alterations [13,14]. Conditional deletion of FTO revealed that metabolic effects of FTO are mainly mediated by neuronal FTO expression, since neuronal-specific FTO depletion recapitulates most of the metabolic phenotype observed in FTO whole body-deficient mice, while hypothalamic depletion of FTO only partially resembled the metabolic effects [88,89]. Thus, these mouse studies show that FTO itself as well as distal genes can both impact metabolism. To date, FTO expression has not been investigated in a mouse model with specific hepatic ablation. However, given the importance of the liver in the regulation of glucose and lipid metabolism, hepatic FTO may play a role in the regulation of these processes. Hepatic *Fto* mRNA levels were increased upon fasting *in vivo* and *in vitro*, while glucose injections reduced *Fto* mRNA levels [90,91]. These studies show correlations between glucose metabolism and hepatic *Fto* expression; however, the extent to which hepatic FTO regulates metabolism

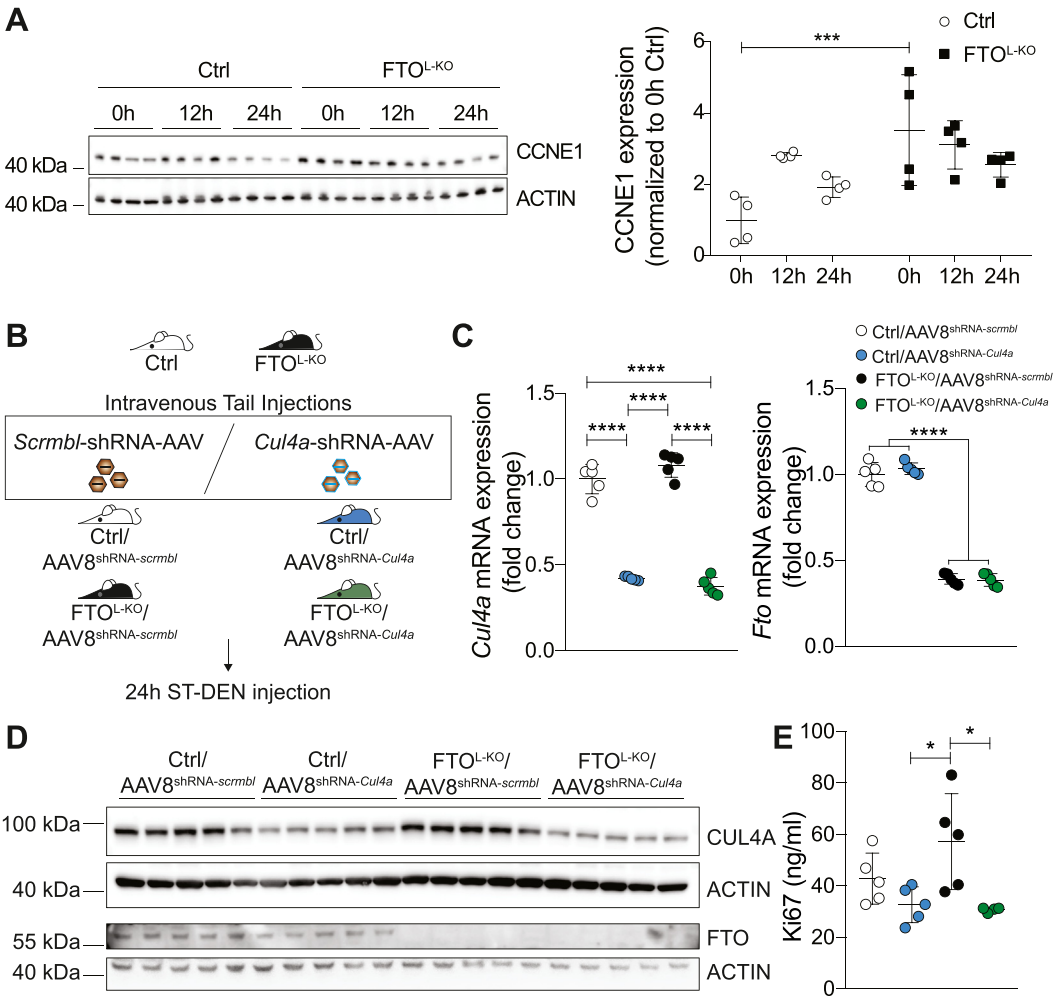

Figure 4: CUL4A knockdown rescues elevated proliferation of livers of FTO^{L-KO} mice. (A) Western blot analyses of CCNE1 in whole liver lysates isolated from ST-DEN injected Ctrl and FTO^{L-KO} mice (n = 4 for each timepoint, two-way ANOVA). CCNE1/β-ACTIN ratio normalized to 0 h Ctrl expression. (B) Scheme of intravenous tail vain injections and different experimental mice groups. (C) qRT-PCR analysis of *Cul4a* and *Fto* expression in whole liver of 24 h ST-DEN injected Ctrl/AAV8$^{shRNA-scrmbl}$, Ctrl/AAV8$^{shRNA-Cul4a}$, FTO^{L-KO}/AAV8$^{shRNA-scrmbl}$, and FTO^{L-KO}/AAV8$^{shRNA-Cul4a}$ (n = 5, one-way ANOVA). (D) Western blot analysis of CUL4A and FTO in whole liver lysates isolated from 24 h ST-DEN-injected Ctrl/AAV8$^{shRNA-scrmbl}$, Ctrl/AAV8$^{shRNA-Cul4a}$, FTO^{L-KO}/AAV8$^{shRNA-scrmbl}$, and FTO^{L-KO}/AAV8$^{shRNA-Cul4a}$ (n = 5). (E) Ki67 ELISA with liver proteins isolated from 24 h ST-DEN-injected Ctrl/AAV8$^{shRNA-scrmbl}$, Ctrl/AAV8$^{shRNA-Cul4a}$, FTO^{L-KO}/AAV8$^{shRNA-scrmbl}$, and FTO^{L-KO}/AAV8$^{shRNA-Cul4a}$ (n = 4–5, one-way ANOVA). p* 0.05, p**** 0.0001. Data are means with SD.

remains to be investigated. Therefore, we performed extensive metabolic phenotyping in untreated FTO^{L-KO} mice. In contrast to the above-mentioned studies, we show that hepatocyte-specific FTO depletion fails to affect body weight, fat mass, WAT and liver weight, glucose metabolism, and key parameters of energy metabolism. However, body weight, fat mass, and WAT weight are reduced in long-term DEN-injected FTO^{L-KO} mice when compared to Ctrl mice. Given the unaltered metabolic phenotype in untreated FTO^{L-KO} mice, those changes are most likely due to enhanced tumor formation in the FTO^{L-KO} mice, rather than a direct metabolic regulatory function of FTO. Of note, metabolic analysis of untreated mice was performed at earlier time points. Therefore, it would also be interesting to investigate metabolic parameters in untreated mice at later time points.

Given the previously demonstrated role of m^{6}A/m^{6}Am mRNA modifications on the initiation and progression of various cancers in general and on HCC specifically [40], we set out to investigate the function of hepatic FTO in HCC development. Our findings show that FTO function protects against chemically-induced HCC development, since FTO^{L-KO} mice display significantly increased tumor burden. Moreover, FTO-deficient, tumor-bearing livers tend to have increased proliferation. In line with our study, HCC patients frequently display increased levels of m^{6}A mRNA modifications accompanied with increased methyltransferase METTL3 expression [57]. METTL3-overexpressing HepG2 cells show increased proliferative potential in a xenograft model of tumor development, further supporting our findings of increased proliferation in the livers of FTO^{L-KO} mice during the tumor initiation phase [57]. Hence, high m^{6}A mRNA modifications increase proliferation in those settings. In contrast, Ma et al. identified decreased m^{6}A mRNA modifications in human metastatic HCC, which is presumably due to reduced METTL14 expression in tumor tissue [58]. However, they also found decreased FTO expression levels in these tissues, further supporting a role for FTO in human HCC.

To investigate the tumor initiation phase in Ctrl and FTO^{L-KO} mice, ST-DEN injections were performed, and the injected mice were sacrificed at different time points after injection. Surprisingly, we found a dynamic regulation of *Fto* mRNA and FTO protein after ST-DEN injections

in livers of Ctrl mice, which expectedly was absent in FTO^{L-KO} livers. To identify downstream targets of the elevated hepatic FTO expression at 24 h after ST-DEN injection in the Ctrl livers, we performed quantitative proteomics and screened for peptides, whose expression correlated or reversely correlated with FTO expression. Strikingly, CUL4A was downregulated in Ctrl livers at 24h post ST-DEN injection, whereas it remained unchanged at all time points in liver lysates from FTO^{L-KO} mice, thereby reversely correlating with FTO expression in Ctrl livers. However, *Cul4a* mRNA expression levels remained unchanged between the genotypes upon ST-DEN injection. This indicates that *Cul4a* mRNA modulated by FTO in Ctrl livers may affect translation rather than transcription. Indeed, m^{6}A/m^{6}Am have been associated with enhanced mRNA stability and translation. In detail, after the 5′ cap structure +1 m^{6}Am-initiated mRNAs were shown to be more stable than mRNAs, which begin with other nucleotides, due to resistance to the mRNA-decapping enzyme DCP2 [29]. However, publicly available miCLIP data on FTO-deficient liver RNA failed to identify m^{6}Am modifications in *Cul4a* transcript [82]. m^{6}A modifications, which are enriched near the 3′ UTR and the STOP codon region, have been shown to be preferably translated via YTHDF1-mediated translation promotion [22,29,92]. To find the specific m^{6}A/m^{6}Am site, which may be demethylated by FTO upon chemically induced liver damage, meRIP and subsequent qRT-PCR was performed with different probes, specific for exons throughout the *Cul4a* mRNA. However, only exon 20 showed significant enrichment after meRIP in FTO-deficient livers after 24 h ST-DEN injection, suggesting that this exon is hypermethylated. m^{6}A modifications enhance mRNA translation, which suggests an elevated translation of the hypermethylated *Cul4a* mRNA in FTO-deficient livers, consequently causing elevated CUL4A protein levels observed in our proteomics screen. However, our experimental set-up does not allow discrimination of whether 2415m^{6}A of *Cul4a* transcript is indeed demethylated by FTO. Mauer et al. recently described that FTO demethylates m^{6}Am on snRNAs, which is supported by the nuclear localization of FTO [23]. snRNAs, which are core components of the spliceosome, can mediate alternative splicing. Thus, differential CUL4A protein levels in FTO^{L-KO} mice upon ST-DEN injection may additionally be caused by altered patterns of alternative splicing of *Cul4a* mRNA, mediated by FTO-dependent m^{6}Am demethylation of snRNAs. Further experiments are needed to ultimately determine why and how CUL4A protein is increased in FTO-deficient livers upon liver damage. However, CUL4A expression and function has been previously linked to HCC development and progression. The scaffold protein CUL4A binds the DNA damage binding protein 1 (DDB1) and the ring of cullins (ROC) to assemble an E3 ubiquitin ligase complex. This E3 ubiquitin ligase has important functions, including regulation of the cell cycle, DNA replication, genomic stability, hematopoiesis, and spermatogenesis [83]. CUL4A is not only upregulated in several HCC cell lines, but also in human HCC samples [84]. Additionally, CUL4A expression positively correlates with hepatocyte proliferation, while an inverse correlation was found regarding tumor differentiation grade and patient survival [84,85]. Indeed, we found a dysregulation of CCNE/Cyclin E1, which activates CDK2 and thus induces G0/G1 to S-phase transition, in FTO^{L-KO} livers when compared to the Ctrl mice [93]. Moreover, CUL4A has been shown to regulate G0/G1 to S-phase transition directly [83]. Hence, these data point to increased cell cycle progression accompanied by enhanced proliferation in FTO^{L-KO} livers upon chemically-induced liver damage. Therefore, we investigated the effect of simultaneous CUL4A knockdown in FTO^{L-KO} mice on proliferation. Indeed, additional knockdown of CUL4A is sufficient to completely restore the elevated Ki67 levels of FTO^{L-KO} during the tumor initiation phase.

Collectively, our study reveals a protective role of FTO against chemically-induced HCC development. We demonstrate that FTO plays a major role during the initiation phase of tumor development, where it is dynamically upregulated upon acute liver damage. Moreover, FTO might target *Cul4a* mRNA to decrease CUL4A protein levels, thereby presumably blocking cell cycle progression and proliferation. Thus, the FTO-CUL4A axis could represent a promising target for developing novel therapeutic approaches to treat HCC.

AUTHOR CONTRIBUTIONS

M.J.M., K.S., H.N., L.K., and L.M. conducted the experiments; M.J.M., R.T.U., J.C.B., and F.T.W. designed the experiments, M.J.M., J.C.B, and F.T.W. wrote the paper. J.Z. and S.-B.Q. assisted meRIP-seq analysis.

ACKNOWLEDGMENTS

The authors thank Jens Alber, Catherina Baitzel, Anke Lietzau, Patrick Jankowski, and Heike Krämer for excellent technical assistance and Pia Scholl, Nadine Spenrath, and Christiane Schäfer for histological stainings. This work was supported by grants from the German Cancer Aid and CECAD to F.T.W. as well as from the Cologne Graduate School for Ageing Research to M.J.M.

CONFLICT OF INTEREST

The authors declare no competing interests.

APPENDIX A. SUPPLEMENTARY DATA

Supplementary data to this article can be found online at https://doi.org/10.1016/j.molmet.2020.101085.

REFERENCES

[1] WHO, 2016. Obesity and Overweight. who.int.
[2] Ford, E.S., Williamson, D.F., Liu, S., 1997. Weight change and diabetes incidence: findings from a national cohort of US adults. American Journal of Epidemiology 146(3):214–222.
[3] Resnick, H.E., Valsania, P., Halter, J.B., Lin, X., 2000. Relation of weight gain and weight loss on subsequent diabetes risk in overweight adults. Journal of Epidemiology & Community Health 54(8):596–602.
[4] Calle, E.E., Rodriguez, C., Walker-Thurmond, K., Thun, M.J., 2003. Overweight, obesity, and mortality from cancer in a prospectively studied cohort of U.S. adults. New England Journal of Medicine 348(17):1625–1638.
[5] Meschia, J.F., Bushnell, C., Boden-Albala, B., Braun, L.T., Bravata, D.M., Chaturvedi, S., et al., 2014. Guidelines for the primary prevention of stroke: a statement for healthcare professionals from the American Heart Association/American Stroke Association. Stroke 45(12):3754–3832.
[6] Lew, E.A., Garfinkel, L., 1979. Variations in mortality by weight among 750,000 men and women. Journal of Chronic Diseases 32(8):563–576.
[7] GLOBOCAN, 2018. International agency for Research on cancer (IARC). Available at: https://gco.iarc.fr/2018.
[8] WHO, W.H.O.M.D., 2008.
[9] Scott, L.J., Mohlke, K.L., Bonnycastle, L.L., Willer, C.J., Li, Y., Duren, W.L., et al., 2007. A genome-wide association study of type 2 diabetes in Finns detects multiple susceptibility variants. Science 316(5829):1341–1345.

[10] Frayling, T.M., Timpson, N.J., Weedon, M.N., Zeggini, E., Freathy, R.M., Lindgren, C.M., et al., 2007. A common variant in the FTO gene is associated with body mass index and predisposes to childhood and adult obesity. Science 316(5826):889–894.
[11] Dina, C., Meyre, D., Gallina, S., Durand, E., Korner, A., Jacobson, P., et al., 2007. Variation in FTO contributes to childhood obesity and severe adult obesity. Nature Genetics 39(6):724–726.
[12] Thorleifsson, G., Walters, G.B., Gudbjartsson, D.F., Steinthorsdottir, V., Sulem, P., Helgadottir, A., et al., 2009. Genome-wide association yields new sequence variants at seven loci that associate with measures of obesity. Nature Genetics 41(1):18–24.
[13] Fischer, J., Koch, L., Emmerling, C., Vierkotten, J., Peters, T., Bruning, J.C., et al., 2009. Inactivation of the Fto gene protects from obesity. Nature 458(7240):894–898.
[14] Church, C., Moir, L., McMurray, F., Girard, C., Banks, G.T., Teboul, L., et al., 2010. Overexpression of Fto leads to increased food intake and results in obesity. Nature Genetics 42(12):1086–1092.
[15] Smemo, S., Tena, J.J., Kim, K.H., Gamazon, E.R., Sakabe, N.J., Gomez-Marin, C., et al., 2014. Obesity-associated variants within FTO form long-range functional connections with IRX3. Nature 507(7492):371–375.
[16] Stratigopoulos, G., Padilla, S.L., LeDuc, C.A., Watson, E., Hattersley, A.T., McCarthy, M.I., et al., 2008. Regulation of Fto/Ftm gene expression in mice and humans. American Journal of Physiology - Regulatory, Integrative and Comparative Physiology 294(4):R1185–R1196.
[17] Stratigopoulos, G., LeDuc, C.A., Cremona, M.L., Chung, W.K., Leibel, R.L., 2011. Cut-like homeobox 1 (CUX1) regulates expression of the fat mass and obesity-associated and retinitis pigmentosa GTPase regulator-interacting protein-1-like (RPGRIP1L) genes and coordinates leptin receptor signaling. Journal of Biological Chemistry 286(3):2155–2170.
[18] Stratigopoulos, G., Martin Carli, J.F., O'Day, D.R., Wang, L., Leduc, C.A., Lanzano, P., et al., 2014. Hypomorphism for RPGRIP1L, a ciliary gene vicinal to the FTO locus, causes increased adiposity in mice. Cell Metabolism 19(5): 767–779.
[19] Gerken, T., Girard, C.A., Tung, Y.C., Webby, C.J., Saudek, V., Hewitson, K.S., et al., 2007. The obesity-associated FTO gene encodes a 2-oxoglutarate-dependent nucleic acid demethylase. Science 318(5855):1469–1472.
[20] Han, Z., Niu, T., Chang, J., Lei, X., Zhao, M., Wang, Q., et al., 2010. Crystal structure of the FTO protein reveals basis for its substrate specificity. Nature 464(7292):1205–1209.
[21] Jia, G., Fu, Y., Zhao, X., Dai, Q., Zheng, G., Yang, Y., et al., 2011. N6-methyladenosine in nuclear RNA is a major substrate of the obesity-associated FTO. Nature Chemical Biology 7(12):885–887.
[22] Meyer, K.D., Saletore, Y., Zumbo, P., Elemento, O., Mason, C.E., Jaffrey, S.R., 2012. Comprehensive analysis of mRNA methylation reveals enrichment in 3' UTRs and near stop codons. Cell 149(7):1635–1646.
[23] Mauer, J., Sindelar, M., Despic, V., Guez, T., Hawley, B.R., Vasseur, J.J., et al., 2019. FTO controls reversible m(6)Am RNA methylation during snRNA biogenesis. Nature Chemical Biology 15(4):340–347.
[24] Mauer, J., Luo, X., Blanjoie, A., Jiao, X., Grozhik, A.V., Patil, D.P., et al., 2017. Reversible methylation of m(6)Am in the 5' cap controls mRNA stability. Nature 541(7637):371–375.
[25] Machnicka, M.A., Milanowska, K., Osman Oglou, O., Purta, E., Kurkowska, M., Olchowik, A., et al., 2013. MODOMICS: a database of RNA modification pathways–2013 update. Nucleic Acids Research 41(Database issue):D262–D267.
[26] Dominissini, D., Moshitch-Moshkovitz, S., Schwartz, S., Salmon-Divon, M., Ungar, L., Osenberg, S., et al., 2012. Topology of the human and mouse m6A RNA methylomes revealed by m6A-seq. Nature 485(7397):201–206.
[27] Deng, X., Su, R., Weng, H., Huang, H., Li, Z., Chen, J., 2018. RNA N(6)-methyladenosine modification in cancers: current status and perspectives. Cell Research 28(5):507–517.
[28] Wang, X., Lu, Z., Gomez, A., Hon, G.C., Yue, Y., Han, D., et al., 2014. N6-methyladenosine-dependent regulation of messenger RNA stability. Nature 505(7481):117–120.
[29] Wang, X., Zhao, B.S., Roundtree, I.A., Lu, Z., Han, D., Ma, H., et al., 2015. N(6)-methyladenosine modulates messenger RNA translation efficiency. Cell 161(6):1388–1399.
[30] Shi, H., Wang, X., Lu, Z., Zhao, B.S., Ma, H., Hsu, P.J., et al., 2017. YTHDF3 facilitates translation and decay of N(6)-methyladenosine-modified RNA. Cell Research 27(3):315–328.
[31] Xiao, W., Adhikari, S., Dahal, U., Chen, Y.S., Hao, Y.J., Sun, B.F., et al., 2016. Nuclear m(6)A reader YTHDC1 regulates mRNA splicing. Molecular Cell 61(4): 507–519.
[32] Huang, H., Weng, H., Sun, W., Qin, X., Shi, H., Wu, H., et al., 2018. Recognition of RNA N(6)-methyladenosine by IGF2BP proteins enhances mRNA stability and translation. Nature Cell Biology 20(3):285–295.
[33] Zhao, B.S., Roundtree, I.A., He, C., 2017. Post-transcriptional gene regulation by mRNA modifications. Nature Reviews Molecular Cell Biology 18(1):31–42.
[34] Zheng, G., Dahl, J.A., Niu, Y., Fedorcsak, P., Huang, C.M., Li, C.J., et al., 2013. ALKBH5 is a mammalian RNA demethylase that impacts RNA metabolism and mouse fertility. Molecular Cell 49(1):18–29.
[35] McTaggart, J.S., Lee, S., Iberl, M., Church, C., Cox, R.D., Ashcroft, F.M., 2011. FTO is expressed in neurones throughout the brain and its expression is unaltered by fasting. PloS One 6(11):e27968.
[36] Hess, M.E., Hess, S., Meyer, K.D., Verhagen, L.A., Koch, L., Bronneke, H.S., et al., 2013. The fat mass and obesity associated gene (Fto) regulates activity of the dopaminergic midbrain circuitry. Nature Neuroscience 16(8):1042–1048.
[37] Ruud, J., Alber, J., Tokarska, A., Engstrom Ruud, L., Nolte, H., Biglari, N., et al., 2019. The fat mass and obesity-associated protein (FTO) regulates locomotor responses to novelty via D2R medium spiny neurons. Cell Reports 27(11):3182–3198 e9.
[38] Ezkurdia, I., Juan, D., Rodriguez, J.M., Frankish, A., Diekhans, M., Harrow, J., et al., 2014. Multiple evidence strands suggest that there may be as few as 19,000 human protein-coding genes. Human Molecular Genetics 23(22): 5866–5878.
[39] The human protein atlas, 2019. Available from: https://www.proteinatlas.org/.
[40] Sun, T., Wu, R., Ming, L., 2019. The role of m6A RNA methylation in cancer. Biomedicine & Pharmacotherapy 112:108613.
[41] Cui, Q., Shi, H., Ye, P., Li, L., Qu, Q., Sun, G., et al., 2017. m(6)A RNA methylation regulates the self-renewal and tumorigenesis of glioblastoma stem cells. Cell Reports 18(11):2622–2634.
[42] Visvanathan, A., Patil, V., Arora, A., Hegde, A.S., Arivazhagan, A., Santosh, V., et al., 2018. Essential role of METTL3-mediated m(6)A modification in glioma stem-like cells maintenance and radioresistance. Oncogene 37(4):522–533.
[43] Zhang, S., Zhao, B.S., Zhou, A., Lin, K., Zheng, S., Lu, Z., et al., 2017. m(6)A demethylase ALKBH5 maintains tumorigenicity of glioblastoma stem-like cells by sustaining FOXM1 expression and cell proliferation program. Cancer Cell 31(4):591–606 e6.
[44] Vu, L.P., Pickering, B.F., Cheng, Y., Zaccara, S., Nguyen, D., Minuesa, G., et al., 2017. The N(6)-methyladenosine (m(6)A)-forming enzyme METTL3 controls myeloid differentiation of normal hematopoietic and leukemia cells. Nature Medicine 23(11):1369–1376.
[45] Weng, H., Huang, H., Wu, H., Qin, X., Zhao, B.S., Dong, L., et al., 2018. METTL14 inhibits hematopoietic stem/progenitor differentiation and promotes leukemogenesis via mRNA m(6)A modification. Cell Stem Cell 22(2):191–205 e9.
[46] Li, Z., Weng, H., Su, R., Weng, X., Zuo, Z., Li, C., et al., 2017. FTO plays an oncogenic role in acute myeloid leukemia as a N(6)-methyladenosine RNA demethylase. Cancer Cell 31(1):127–141.
[47] Su, R., Dong, L., Li, C., Nachtergaele, S., Wunderlich, M., Qing, Y., et al., 2018. R-2HG exhibits anti-tumor activity by targeting FTO/m(6)A/MYC/CEBPA signaling. Cell 172(1–2):90–105 e23.

[48] Kwok, C.T., Marshall, A.D., Rasko, J.E., Wong, J.J., 2017. Genetic alterations of m(6)A regulators predict poorer survival in acute myeloid leukemia. Journal of Hematology & Oncology 10(1):39.

[49] Zhang, C., Samanta, D., Lu, H., Bullen, J.W., Zhang, H., Chen, I., et al., 2016. Hypoxia induces the breast cancer stem cell phenotype by HIF-dependent and ALKBH5-mediated m(6)A-demethylation of NANOG mRNA. Proceedings of the National Academy of Sciences of the United States of America 113(14): E2047–E2056.

[50] Zhang, C., Zhi, W.I., Lu, H., Samanta, D., Chen, I., Gabrielson, E., et al., 2016. Hypoxia-inducible factors regulate pluripotency factor expression by ZNF217- and ALKBH5-mediated modulation of RNA methylation in breast cancer cells. Oncotarget 7(40):64527–64542.

[51] Cai, X., Wang, X., Cao, C., Gao, Y., Zhang, S., Yang, Z., et al., 2018. HBXIP-elevated methyltransferase METTL3 promotes the progression of breast cancer via inhibiting tumor suppressor let-7g. Cancer Letters 415:11–19.

[52] He, Y., Hu, H., Wang, Y., Yuan, H., Lu, Z., Wu, P., et al., 2018. ALKBH5 inhibits pancreatic cancer motility by decreasing long non-coding RNA KCNK15-AS1 methylation. Cellular Physiology and Biochemistry 48(2):838–846.

[53] Chen, J., Sun, Y., Xu, X., Wang, D., He, J., Zhou, H., et al., 2017. YTH domain family 2 orchestrates epithelial-mesenchymal transition/proliferation dichotomy in pancreatic cancer cells. Cell Cycle 16(23):2259–2271.

[54] Li, J., Meng, S., Xu, M., Wang, S., He, L., Xu, X., et al., 2018. Downregulation of N(6)-methyladenosine binding YTHDF2 protein mediated by miR-493-3p suppresses prostate cancer by elevating N(6)-methyladenosine levels. Oncotarget 9(3):3752–3764.

[55] Zhou, S., Bai, Z.L., Xia, D., Zhao, Z.J., Zhao, R., Wang, Y.Y., et al., 2018. FTO regulates the chemo-radiotherapy resistance of cervical squamous cell carcinoma (CSCC) by targeting beta-catenin through mRNA demethylation. Molecular Carcinogenesis 57(5):590–597.

[56] Liu, J., Eckert, M.A., Harada, B.T., Liu, S.M., Lu, Z., Yu, K., et al., 2018. m(6)A mRNA methylation regulates AKT activity to promote the proliferation and tumorigenicity of endometrial cancer. Nature Cell Biology 20(9):1074–1083.

[57] Chen, M., Wei, L., Law, C.T., Tsang, F.H., Shen, J., Cheng, C.L., et al., 2018. RNA N6-methyladenosine methyltransferase-like 3 promotes liver cancer progression through YTHDF2-dependent posttranscriptional silencing of SOCS2. Hepatology 67(6):2254–2270.

[58] Ma, J.Z., Yang, F., Zhou, C.C., Liu, F., Yuan, J.H., Wang, F., et al., 2017. METTL14 suppresses the metastatic potential of hepatocellular carcinoma by modulating N(6) -methyladenosine-dependent primary MicroRNA processing. Hepatology 65(2):529–543.

[59] Yang, Z., Li, J., Feng, G., Gao, S., Wang, Y., Zhang, S., et al., 2017. MicroRNA-145 modulates N(6)-methyladenosine levels by targeting the 3'-untranslated mRNA region of the N(6)-methyladenosine binding YTH domain family 2 protein. Journal of Biological Chemistry 292(9):3614–3623.

[60] Lan, Q., Liu, P.Y., Haase, J., Bell, J.L., Huttelmaier, S., Liu, T., 2019. The critical role of RNA m(6)A methylation in cancer. Cancer Research 79(7): 1285–1292.

[61] Bokar, J.A., Shambaugh, M.E., Polayes, D., Matera, A.G., Rottman, F.M., 1997. Purification and cDNA cloning of the AdoMet-binding subunit of the human mRNA (N6-adenosine)-methyltransferase. RNA 3(11):1233–1247.

[62] Liu, J., Yue, Y., Han, D., Wang, X., Fu, Y., Zhang, L., et al., 2014. A METTL3-METTL14 complex mediates mammalian nuclear RNA N6-adenosine methylation. Nature Chemical Biology 10(2):93–95.

[63] Ping, X.L., Sun, B.F., Wang, L., Xiao, W., Yang, X., Wang, W.J., et al., 2014. Mammalian WTAP is a regulatory subunit of the RNA N6-methyladenosine methyltransferase. Cell Research 24(2):177–189.

[64] Schwartz, S., Mumbach, M.R., Jovanovic, M., Wang, T., Maciag, K., Bushkin, G.G., et al., 2014. Perturbation of m6A writers reveals two distinct classes of mRNA methylation at internal and 5' sites. Cell Reports 8(1): 284–296.

[65] Patil, D.P., Chen, C.K., Pickering, B.F., Chow, A., Jackson, C., Guttman, M., et al., 2016. m(6)A RNA methylation promotes XIST-mediated transcriptional repression. Nature 537(7620):369–373.

[66] Li, J., Zhu, L., Shi, Y., Liu, J., Lin, L., Chen, X., 2019. m6A demethylase FTO promotes hepatocellular carcinoma tumorigenesis via mediating PKM2 demethylation. American Journal of Translational Research 11(9):6084–6092.

[67] Dubiel, D., Bintig, W., Kahne, T., Dubiel, W., Naumann, M., 2017. Cul3 neddylation is crucial for gradual lipid droplet formation during adipogenesis. Biochimica et Biophysica Acta (BBA) - Molecular Cell Research 1864(8):1405–1412.

[68] Schneider, C.A., Rasband, W.S., Eliceiri, K.W., 2012. NIH Image to ImageJ: 25 years of image analysis. Nature Methods 9(7):671–675.

[69] Rappsilber, J., Ishihama, Y., Mann, M., 2003. Stop and go extraction tips for matrix-assisted laser desorption/ionization, nanoelectrospray, and LC/MS sample pretreatment in proteomics. Analytical Chemistry 75(3):663–670.

[70] Cox, J., Mann, M., 2008. MaxQuant enables high peptide identification rates, individualized p.p.b.-range mass accuracies and proteome-wide protein quantification. Nature Biotechnology 26(12):1367–1372.

[71] Cox, J., Neuhauser, N., Michalski, A., Scheltema, R.A., Olsen, J.V., Mann, M., 2011. Andromeda: a peptide search engine integrated into the MaxQuant environment. Journal of Proteome Research 10(4):1794–1805.

[72] Nolte, H., MacVicar, T.D., Tellkamp, F., Kruger, M., 2018. Instant Clue: a software suite for interactive data visualization and analysis. Scientific Reports 8(1):12648.

[73] Perez-Riverol, Y., Csordas, A., Bai, J., Bernal-Llinares, M., Hewapathirana, S., Kundu, D.J., et al., 2019. The PRIDE database and related tools and resources in 2019: improving support for quantification data. Nucleic Acids Research 47(D1):D442–D450.

[74] Xiao, Y., Wang, Y., Tang, Q., Wei, L., Zhang, X., Jia, G., 2018. An elongation- and ligation-based qPCR amplification method for the radiolabeling-free detection of locus-specific N(6) -methyladenosine modification. Angewandte Chemie International Edition in English 57(49):15995–16000.

[75] Kellendonk, C., Opherk, C., Anlag, K., Schutz, G., Tronche, F., 2000. Hepatocyte-specific expression of Cre recombinase. Genesis 26(2):151–153.

[76] Guo, J., Ren, W., Li, A., Ding, Y., Guo, W., Su, D., et al., 2013. Fat mass and obesity-associated gene enhances oxidative stress and lipogenesis in nonalcoholic fatty liver disease. Digestive Diseases and Sciences 58(4): 1004–1009.

[77] Kang, H., Zhang, Z., Yu, L., Li, Y., Liang, M., Zhou, L., 2018. FTO reduces mitochondria and promotes hepatic fat accumulation through RNA demethylation. Journal of Cellular Biochemistry 119(7):5676–5685.

[78] Lim, A., Zhou, J., Sinha, R.A., Singh, B.K., Ghosh, S., Lim, K.H., et al., 2016. Hepatic FTO expression is increased in NASH and its silencing attenuates palmitic acid-induced lipotoxicity. Biochemical and Biophysical Research Communications 479(3):476–481.

[79] Jones, A., Friedrich, K., Rohm, M., Schafer, M., Algire, C., Kulozik, P., et al., 2013. TSC22D4 is a molecular output of hepatic wasting metabolism. EMBO Molecular Medicine 5(2):294–308.

[80] Schafer, M., Oeing, C.U., Rohm, M., Baysal-Temel, E., Lehmann, L.H., Bauer, R., et al., 2016. Ataxin-10 is part of a cachexokine cocktail triggering cardiac metabolic dysfunction in cancer cachexia. Molecular Metabolism 5(2):67–78.

[81] Zhou, J., Wan, J., Shu, X.E., Mao, Y., Liu, X.M., Yuan, X., et al., 2018. N(6)-Methyladenosine guides mRNA alternative translation during integrated stress response. Molecular Cell 69(4):636–647 e7.

[82] Linder, B., Grozhik, A.V., Olarerin-George, A.O., Meydan, C., Mason, C.E., Jaffrey, S.R., 2015. Single-nucleotide-resolution mapping of m6A and m6Am throughout the transcriptome. Nature Methods 12(8):767–772.

[83] Sharma, P., Nag, A., 2014. CUL4A ubiquitin ligase: a promising drug target for cancer and other human diseases. Open Biology 4:130217.

[84] Yasui, K., Arii, S., Zhao, C., Imoto, I., Ueda, M., Nagai, H., et al., 2002. TFDP1, CUL4A, and CDC16 identified as targets for amplification at 13q34 in hepatocellular carcinomas. Hepatology 35(6):1476—1484.

[85] Pan, Y., Wang, B., Yang, X., Bai, F., Xu, Q., Li, X., et al., 2015. CUL4A facilitates hepatocarcinogenesis by promoting cell cycle progression and epithelial-mesenchymal transition. Scientific Reports 5:17006.

[86] Higa, L.A., Yang, X., Zheng, J., Banks, D., Wu, M., Ghosh, P., et al., 2006. Involvement of CUL4 ubiquitin E3 ligases in regulating CDK inhibitors Dacapo/p27Kip1 and cyclin E degradation. Cell Cycle 5(1):71—77.

[87] Boissel, S., Reish, O., Proulx, K., Kawagoe-Takaki, H., Sedgwick, B., Yeo, G.S., et al., 2009. Loss-of-function mutation in the dioxygenase-encoding FTO gene causes severe growth retardation and multiple malformations. The American Journal of Human Genetics 85(1):106—111.

[88] McMurray, F., Church, C.D., Larder, R., Nicholson, G., Wells, S., Teboul, L., et al., 2013. Adult onset global loss of the fto gene alters body composition and metabolism in the mouse. PLoS Genetics 9(1):e1003166.

[89] Gao, X., Shin, Y.H., Li, M., Wang, F., Tong, Q., Zhang, P., 2010. The fat mass and obesity associated gene FTO functions in the brain to regulate postnatal growth in mice. PloS One 5(11):e14005.

[90] Poritsanos, N.J., Lew, P.S., Mizuno, T.M., 2010. Relationship between blood glucose levels and hepatic Fto mRNA expression in mice. Biochemical and Biophysical Research Communications 400(4):713—717.

[91] Mizuno, T.M., Lew, P.S., Luo, Y., Leckstrom, A., 2017. Negative regulation of hepatic fat mass and obesity associated (Fto) gene expression by insulin. Life Sciences 170:50—55.

[92] Liu, J., Li, K., Cai, J., Zhang, M., Zhang, X., Xiong, X., et al., 2020. Landscape and regulation of m(6)A and m(6)Am methylome across human and mouse tissues. Molecular Cell 77(2):426—440 e6.

[93] Clurman, B.E., Sheaff, R.J., Thress, K., Groudine, M., Roberts, J.M., 1996. Turnover of cyclin E by the ubiquitin-proteasome pathway is regulated by cdk2 binding and cyclin phosphorylation. Genes & Development 10(16):1979—1990.

